small methods
www.small-methods.com

Cycling Rate-Induced Spatially-Resolved Heterogeneities in Commercial Cylindrical Li-Ion Batteries

Antonis Vamvakeros, Dorota Matras, Thomas E. Ashton, Alan A. Coelho, Hongyang Dong, Dustin Bauer, Yaroslav Odarchenko, Stephen W. T. Price, Keith T. Butler, Olof Gutowski, Ann-Christin Dippel, Martin von Zimmerman, Jawwad A. Darr, Simon D. M. Jacques,* and Andrew M. Beale**

Synchrotron high-energy X-ray diffraction computed tomography has been employed to investigate, for the first time, commercial cylindrical Li-ion batteries electrochemically cycled over the two cycling rates of C/2 and C/20. This technique yields maps of the crystalline components and chemical species as a cross-section of the cell with high spatiotemporal resolution (550 × 550 images with 20 × 20 × 3 μm^3 voxel size in ca. 1 h). The recently developed Direct Least-Squares Reconstruction algorithm is used to overcome the well-known parallax problem and led to accurate lattice parameter maps for the device cathode. Chemical heterogeneities are revealed at both electrodes and are attributed to uneven Li and current distributions in the cells. It is shown that this technique has the potential to become an invaluable diagnostic tool for real-world commercial batteries and for their characterization under operating conditions, leading to unique insights into "real" battery degradation mechanisms as they occur.

1. Introduction

Li-ion batteries (LiBs) have dominated the energy storage market finding applications in portable electronic devices, electrical vehicles and grid storage. Their success has been primarily driven by high gravimetric and volumetric energy densities compared to other existing secondary (rechargeable) battery systems such as Ni-metal hydride, Ni-Cd, and Pb-acid batteries. There has been a tremendous growth in LiB research since the first commercial cell produced by the Sony Corporation in the early 90's which incorporated a $LiCoO_2$ layered oxide cathode. Although much of the focus has been on maximizing the power and energy density of cells while minimizing production cost, extending battery life cycle (both operational and calendar) and improving safety (e.g., through sophisticated thermal and current/voltage battery management systems) are equally important for the future of LiBs.[1–5] The current commercially available cathode materials in LiBs are largely based on intercalation-type materials, including 1) layered-type [$LiCoO_2$, $LiNi_{0.33}Mn_{0.33}Co_{0.33}O_2$ (NMC), and $LiNi_{0.8}Co_{0.15}Al_{0.05}O_2$ (NCA)], 2) spinel-type ($LiMn_2O_4$), and 3) olivine-type ($LiFePO_4$) while anode materials typically consist of graphite or $Li_4Ti_5O_{12}$ compounds.[6] The main trend within

A. Vamvakeros, Y. Odarchenko, S. W. T. Price, S. D. M. Jacques, A. M. Beale
Finden Limited
Merchant House, 5 East St Helens Street, Abingdon OX14 5EG, UK
E-mail: antony@finden.co.uk; simon@finden.co.uk

D. Matras
The Faraday Institution
Quad One
Harwell Science and Innovation Campus
Didcot OX11 0RA, UK

D. Matras
Diamond Light Source
Harwell Science and Innovation Campus
Didcot, Oxfordshire OX11 0DE, UK

The ORCID identification number(s) for the author(s) of this article can be found under https://doi.org/10.1002/smtd.202100512.

DOI: 10.1002/smtd.202100512

T. E. Ashton, H. Dong, D. Bauer, J. A. Darr, A. M. Beale
Department of Chemistry
University College London
20 Gordon Street, London WC1H 0AJ, UK
E-mail: andrew.beale@ucl.ac.uk

A. A. Coelho
Coelho Software
72 Cedar Street, Wynnum, Brisbane, Queensland 4178, Australia

K. T. Butler
SciML
Scientific Computer Division
Rutherford Appleton Laboratory
Harwell OX11 0QX, UK

O. Gutowski, A. C. Dippel, M. v. Zimmerman
Deutsches Elektronen-Synchrotron DESY
Notkestraße 85, 22607 Hamburg, Germany

A. M. Beale
Research Complex at Harwell
Rutherford Appleton Laboratory
Harwell Science and Innovation Campus
Didcot, Oxon OX11 0FA, UK

commercial cathode materials focuses on substituting expensive and toxic Co with Ni, leading to NMC and NCA materials containing > 80% of Ni, while the anode materials are moving towards graphite-silicon composites.

The continuing development in LiB technology includes in situ/*operando* studies[7–13] which provide invaluable insight into reactions occurring within the electrode(s) and at the electrode/electrolyte interface. This information is crucial in the understanding of charge storage and degradation mechanisms. The application of X-ray imaging techniques has proven to be a powerful tool for battery material characterization; information regarding chemical composition, electronic structure, and electrode materials morphology can be obtained with high temporal and spatial resolution, especially at synchrotron facilities.[14–35] On the other hand, laboratory sources have been primarily applied for X-ray absorption-contrast imaging (aka. micro-CT),[36–38] reaching high-resolution images (i.e., sub μm) but requiring substantially longer acquisition times (from several to tens of hours). It is important to note that due to the size, thickness and highly absorbing material used for battery casings of commercial cylindrical LiB cells (i.e., steel) only high energy X-rays ≈ 100 keV can be used as a probe. As a result, high-energy X-ray scattering-based and absorption-contrast-based techniques are among the very limited options for non-invasive studies of commercial cells. Additionally, neutrons, having significantly higher penetration depth than X-rays, can also be used to study LiBs.[39–47] Recent developments in neutron diffraction imaging techniques, such as neutron diffraction computed tomography (ND-CT) and direct/real space neutron diffraction imaging,[48–51] have shown that neutron diffraction can be considered as a powerful characterization tool for ex situ measurements.

X-ray diffraction computed tomography (XRD-CT) combines X-ray powder diffraction with a tomographic data collection approach using a monochromatic pencil beam. In contrast to conventional micro-CT, XRD-CT yields a sample cross-section image where each pixel contains rich physico-chemical information, embedded within a local diffraction pattern. It has been demonstrated that spatially-resolved quantitative information regarding the concentration of crystalline phases, their lattice parameters and size of crystallites, can be extracted through full profile analysis approaches, such as the Rietveld method.[52–54] Similar to XRD-CT, a total scattering pattern can be collected while performing a tomographic scan, a technique known as pair distribution function computed tomography (PDF-CT) which provides information regarding short-range order components.[55] However, until now X-ray scattering-based tomography techniques have not been applied to commercial cylindrical LiBs due to challenges in data analysis. The first problem arises from the thick steel layer used in the battery casing which is both a highly absorbing and a highly scattering material. Although tomographic measurements can be used to spatially separate the various sample components in the reconstructed dataset, the high intensity of the steel signal dominates the scattering pattern, leading to artifacts in the reconstructed images/diffraction patterns. The second and more challenging problem is the parallax artifact arising when a relatively large sample is investigated (typically with diameter larger than a few mm). For such cases, X-rays scattered/diffracted at the same scattering angle 2theta along the sample thickness arrive at multiple/different detector elements. The parallax artifact leads to loss of physico-chemical information (i.e., accuracy in crystallite sizes and lattice parameters) when extracted through conventional data analysis approaches (i.e., reconstruction of XRD-CT images and subsequent analysis of the local diffraction signals). Some of the authors have recently developed a new XRD-CT reconstruction algorithm, termed Direct Least-Squares Reconstruction (DLSR) algorithm, which overcomes the parallax artifact[56] and can be applied to reconstruct images from real-world devices, such as commercial LiB cells.

In this work we employ, for the first time, the XRD-CT technique to investigate spatial heterogeneities in terms of distribution of crystalline phases and their lattice parameters inside commercial Li-ion AAA batteries (with nominal capacity of 600 mAh) as a function of electrochemical cell cycling using the current rates of C/2 and C/20 respectively. The distribution of crystalline phases and lattice parameters obtained from these measurements has revealed inhomogeneous charging and discharging behavior in terms of Li distribution at both the anode and cathode.

2. Results

The spatial distribution of all components identified in the pristine cell, obtained through full profile analysis of self-absorption corrected XRD-CT data using the Rietveld method, is presented in **Figure 1**. The main components of the battery cell (i.e., steel casing, Cu current collector, Al current collector, and polymer separator), as well as the cathode and anode materials, were identified in the diffraction data (**Figure 2** and Figures S1–S3, Tables S1–S5, Supporting Information). The active cathode material comprised two $LiNi_{0.5}Mn_{0.3}Co_{0.2}O_2$ (NMC532) layered phases with different unit cell sizes (Figure S3 and Tables S1 and S2, Supporting Information). These phases are mentioned throughout the text as the primary and secondary NMC532 phases respectively. For the primary phase Rietveld refinement indicated ≈ 34 wt.%; the secondary NMC532 phase appears to be minor at a concentration of <1 wt.% (Table S4, Supporting Information). The primary NMC532 phase (P) was uniformly distributed throughout the

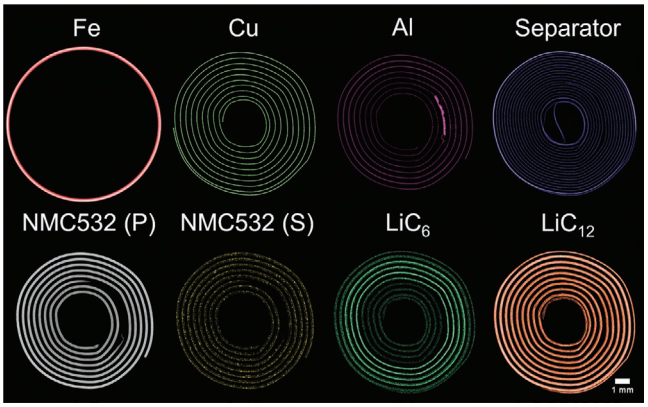

Figure 1. Spatial distribution of all components identified in the pristine AAA battery cell. Note the bracketed letters (P) and (S) indicate the primary and secondary NMC532 components.

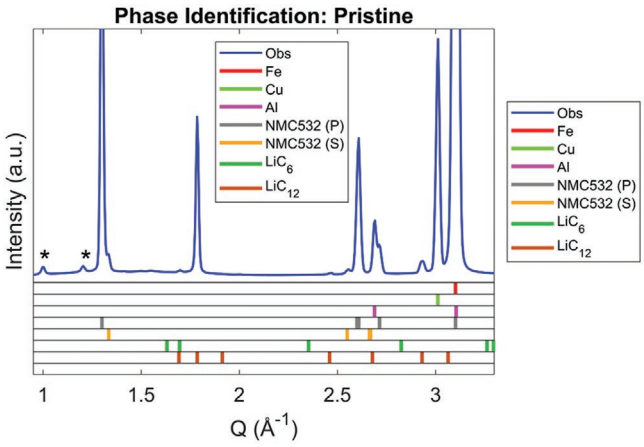

Figure 2. Phase identification of the pristine AAA battery cell using the mean diffraction pattern from the XRD-CT dataset. Blue line: the summed diffraction pattern, Red ticks: Fe (steel casing), Green ticks: Cu current collector, Magenta ticks: Aluminum current collector, Grey ticks: primary NMC532 (P), Orange ticks: secondary NMC532 (S), Darker Green ticks: LiC_6, Brown ticks: LiC_{12}, Asterisks: polymer separator.

cathode, whilst the secondary phase (S) was localized with weight-percents in excess of 20% (Figures S4–S7, Supporting Information). Detection of this secondary phase was possible due to the spatially-resolved nature of the diffraction data and could have been missed in a conventional single-point measurement, as can be seen from the mean XRD-CT diffraction patterns (Figure 2 and Figures S8–S10, Supporting Information). The anode comprised two Li-C phases, LiC_6 and LiC_{12} (Figures S1, S8, and S11, Supporting Information). The LiC_{12} phase was uniformly distributed across and along the anode electrode whereas the LiC_6 phase was present primarily closer to the battery casing than in the middle of the cell. The presence of both LiC_6 and LiC_{12} in the pristine phase is due to the cell being partially charged by the manufacturer. It should be emphasized that in conventional micro-CT, all Li-C phases, the Al current collector, and the polymer separator appear almost/totally transparent due to their low density (Figures S5 and S12–S14, Supporting Information). Similarly, micro-CT is not able to differentiate between the various crystalline phases at the cathode (different chemical species with similar density).

Four Li-ion AAA battery cells from the same manufacturer were electrochemically cycled and then investigated with XRD-CT. Initially, all four AAA batteries were slowly charged using a constant current constant voltage (CCCV) regime to 4.2 V at a slow current rate (C/20); this brings all cells to the same electrochemical state (**Figure 3**a–d). As the cells were pre-charged, a small residual charge capacity ≈80–90 mAh was observed. Subsequently, all four cells were discharged to 2.75 V using two cycling rates, C/20 (Figure 3e) and C/2 (Figure 3f), and then two cells were charged to 4.2 V with C/20 or C/2 cycling rates (corresponding to 40 and 400 mA, respectively). As a result, the obtained cells were: 1) discharged to 2.75 V with C/2 rate, 2) discharged to 2.75 V with C/20 rate, 3) discharged to 2.75 V – charged to 4.2 V with C/2 rate, and 4) discharged to 2.75 V – charged to 4.2 V with C/20 rate. The various cycling rates resulted in significantly different discharge capacities of the pre-cycled cells (45 mAh vs 320–350 mAh for the cells cycled at C/2 and C/20, respectively).

Figure 4 shows phase distribution maps of the crystalline phases present in the anode and cathode layers from the two discharged battery cells. The anode is seen to contain primarily graphite and a partially lithiated graphite phase identified as LiC_{30}, with the latter being in close proximity to the Al current collector, steel casing, and polymer separator in the

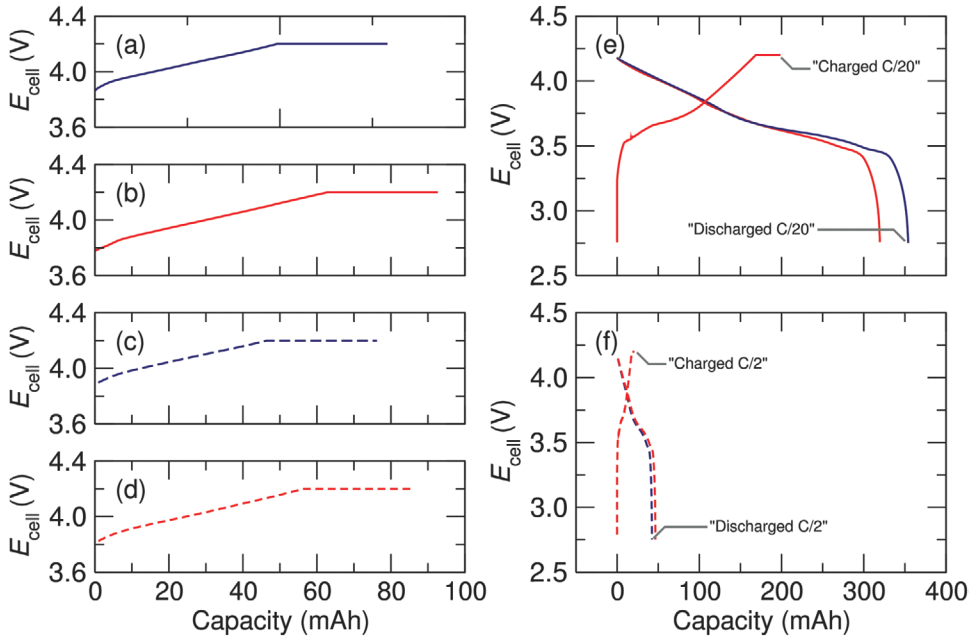

Figure 3. Charge-discharge curves of the four AAA battery cells prepared for XRD-CT measurements. a–d) Initial CCCV charge step for all four cells at C/20. e) Subsequent C/20 charge and discharge steps for the two C/20 cells. f) Subsequent C/2 charge and discharge steps for the two C/2 cells. Labels in (e) and (f) show the final state for each cell prior to XRD-CT analyses.

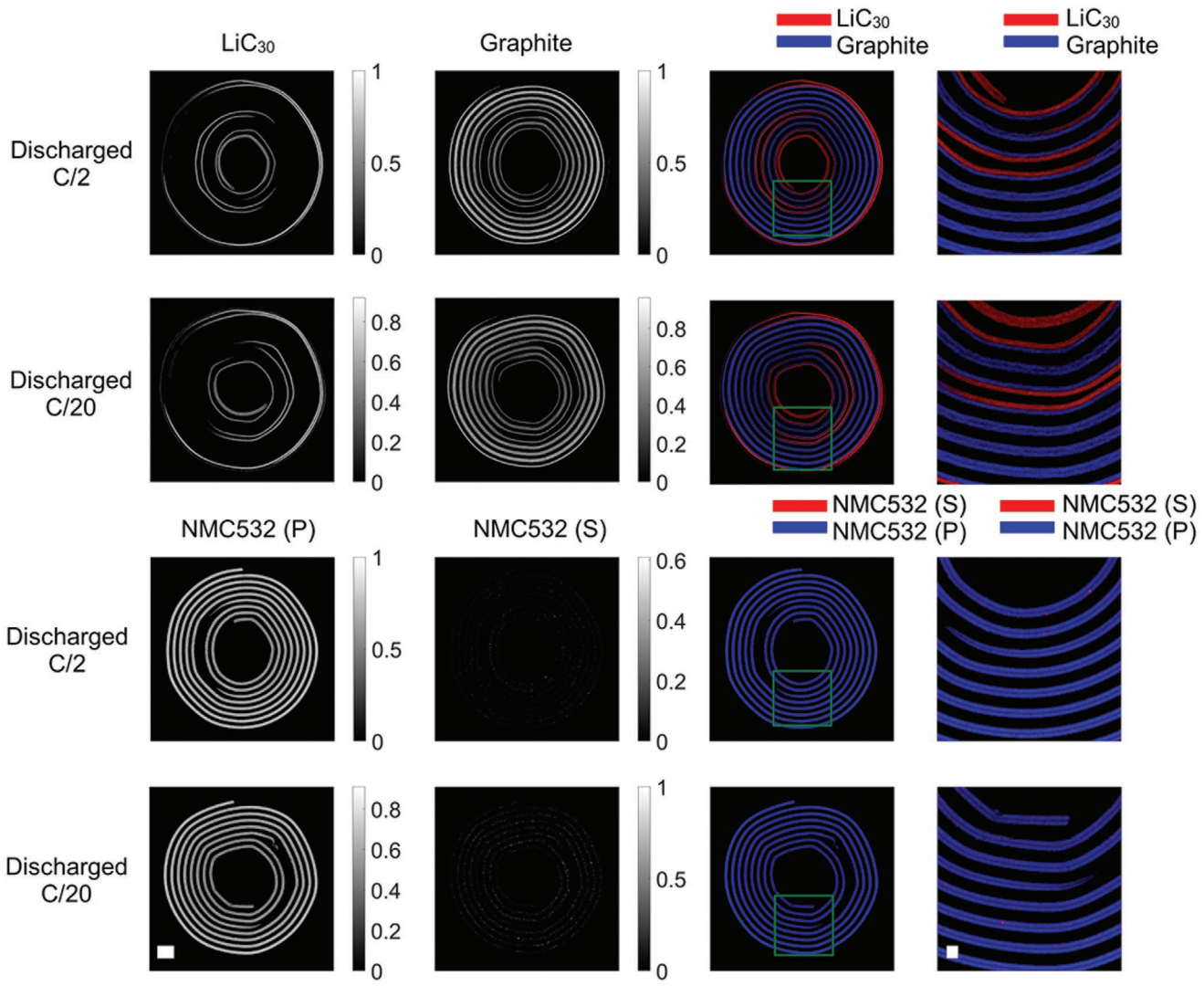

Figure 4. Phase distribution maps of the crystalline phases present in the anode (top panel) and in the cathode (bottom panel) of two charged-discharged cells with different cycling rates (C/2 and C/20). Scale bar in the bottom left corresponds to 1 mm (all electrode maps) and in the bottom right to 0.2 mm (magnified electrode map).

core of the jelly roll (these regions are mentioned throughout the text as Fe-Al-Sep). No significant differences are observed between the two pre-cycled cells regarding the distribution and relative quantity of the anode materials (Table S5, Supporting Information). These results provide direct evidence that the de-lithiation process is not homogeneous in the anode (i.e., it is delayed in the Fe-Al-Sep regions) and that this phenomenon is independent of the cycling rate (Figure S15, Supporting Information). The cathode in both cells is composed of the primary NMC532 phase and a small amount of the secondary NMC532 (ca. 1 wt.% as shown in Table S5, Supporting Information), the latter being present in certain areas of the electrode at high concentrations (i.e., material hotspots). These observations imply that the secondary NMC532 phase could be attributed to a manufacturing/production process (i.e., a result of impurities during manufacturing or a result of the first-cycle irreversible capacity loss) which leads to cells with varying initial concentrations of this component.

The phase distribution maps of the crystalline phases present in the anode and cathode layers, obtained from the analysis of the two XRD-CT datasets from the two discharged-charged battery cells, are presented in **Figure 5**. The most striking difference between these two cells, cycled with different rates (C/2 and C/20 respectively), is the quantity and distribution of the LiC_6 phase. Specifically, the cell cycled at a C/2 rate primarily consists of LiC_{12} with a significantly lower amount of LiC_6. In terms of weight fractions, this difference corresponds to 3.4 wt.% LiC_6 and 21.1 wt.% LiC_{12} in the C/2 cell versus 10.5 wt.% LiC_6 and 13.4 wt.% LiC_{12} in the C/2 cell as shown in Table S4, Supporting Information. Importantly, LiC_6 is primarily present at the surface of the anode layers (red-blue image in the top right of Figure 5); this indicates that under the imposed conditions, the lithiation process is not homogeneous across the thickness of the anode (Figure S15, Supporting Information). As for the cell cycled at the lower rate of C/20, both LiC_6 and LiC_{12} phases were identified, with

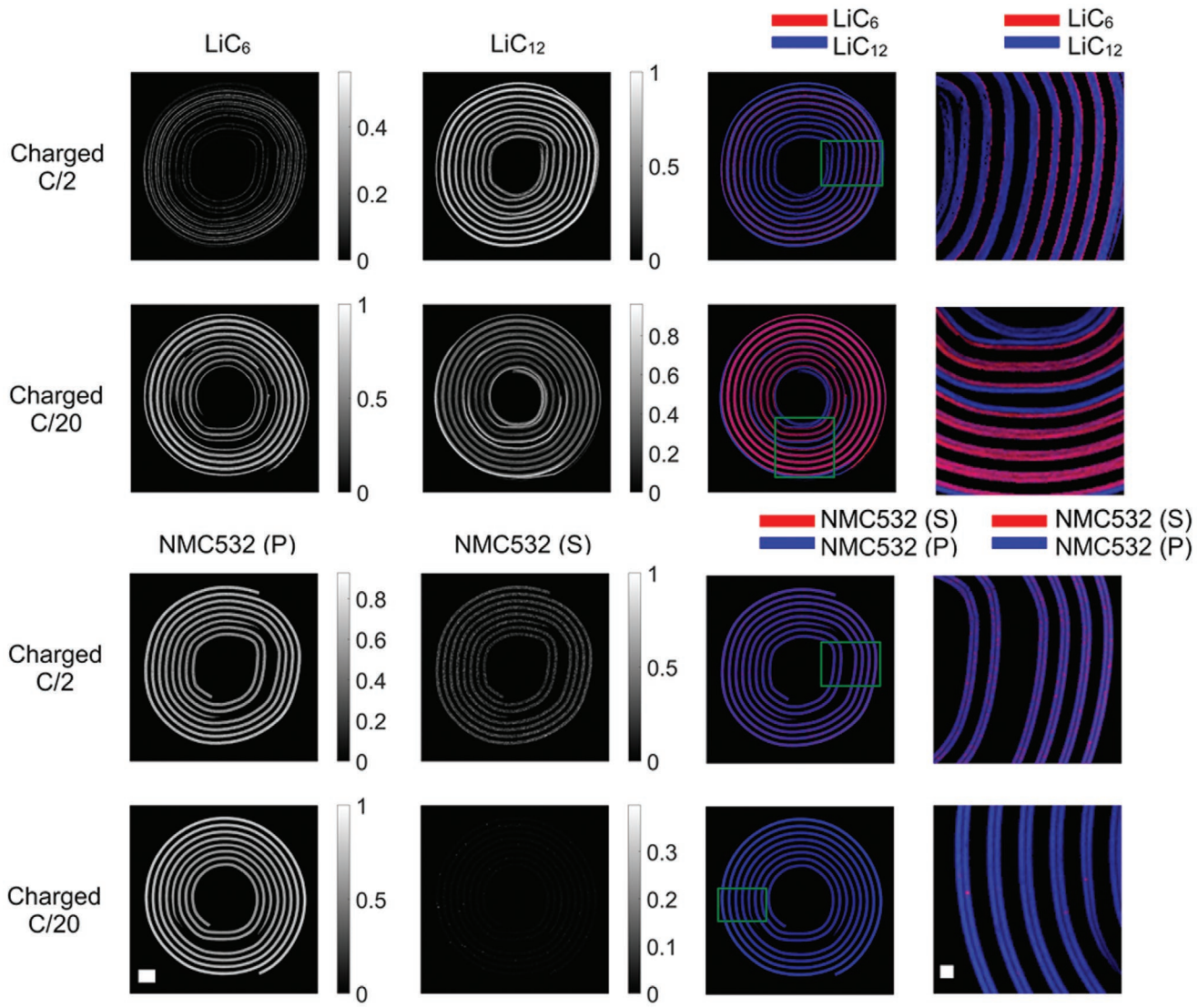

Figure 5. Phase distribution maps of the crystalline phases present in the anode (top panel) and in the cathode (bottom panel) of two charged cells with different cycling rates (C/2 and C/20). Scale bar in the bottom left corresponds to 1 mm (all electrode maps) and in the bottom right to 0.2 mm (magnified electrode map).

the latter being present mainly in electrode regions which are in close proximity to the Al current collectors, steel casing, and polymer separator in the core of the jelly roll (Fe-Al-Sep). Taking into account the results of the two discharged cells presented in Figure 4, it is clearly seen that the lithiation process is delayed in these areas compared to other regions and that this delay takes place both during discharging and charging of the battery.

For the cathode materials, both cells consisted of the primary NMC532 phase uniformly distributed across the electrode layers and a small amount of the secondary NMC532 phase located at regions of high concentration. The cell cycled at the C/20 rate contained significantly less of the secondary phase when compared to the cell cycled at the C/2 rate (i.e., 4.3 wt.% in the C/2 cell vs <1 wt.% in the C/20 cell as shown in Table S4, Supporting Information). Importantly, this phase has almost identical lattice parameters in both the discharged and discharged-charged cells; this demonstrates its inability to participate in the (de)lithiation process and can be considered as an inactive material. However, as mentioned previously, locally the concentration of this inactive material can rise to more than 20 wt.% which can have a significant negative impact on the (de)lithiation process during cycling (e.g., preventing easy access of Li-ions to the active material in the cathode) and the resulting capacity.

Next, the DLSR algorithm was applied to overcome the parallax problem (Figures S16 and S17, Supporting Information) and extract accurate physio-chemical information of the crystalline phases present in the five battery cells (i.e., including the pristine cell).[56] This algorithm is computationally expensive and the data were therefore downscaled by a factor of four (4x). The spatial distributions of the *a* and *c* lattice parameters of the hexagonal NMC532 phase are presented in **Figure 6**. The mean values and their standard deviation are summarized in

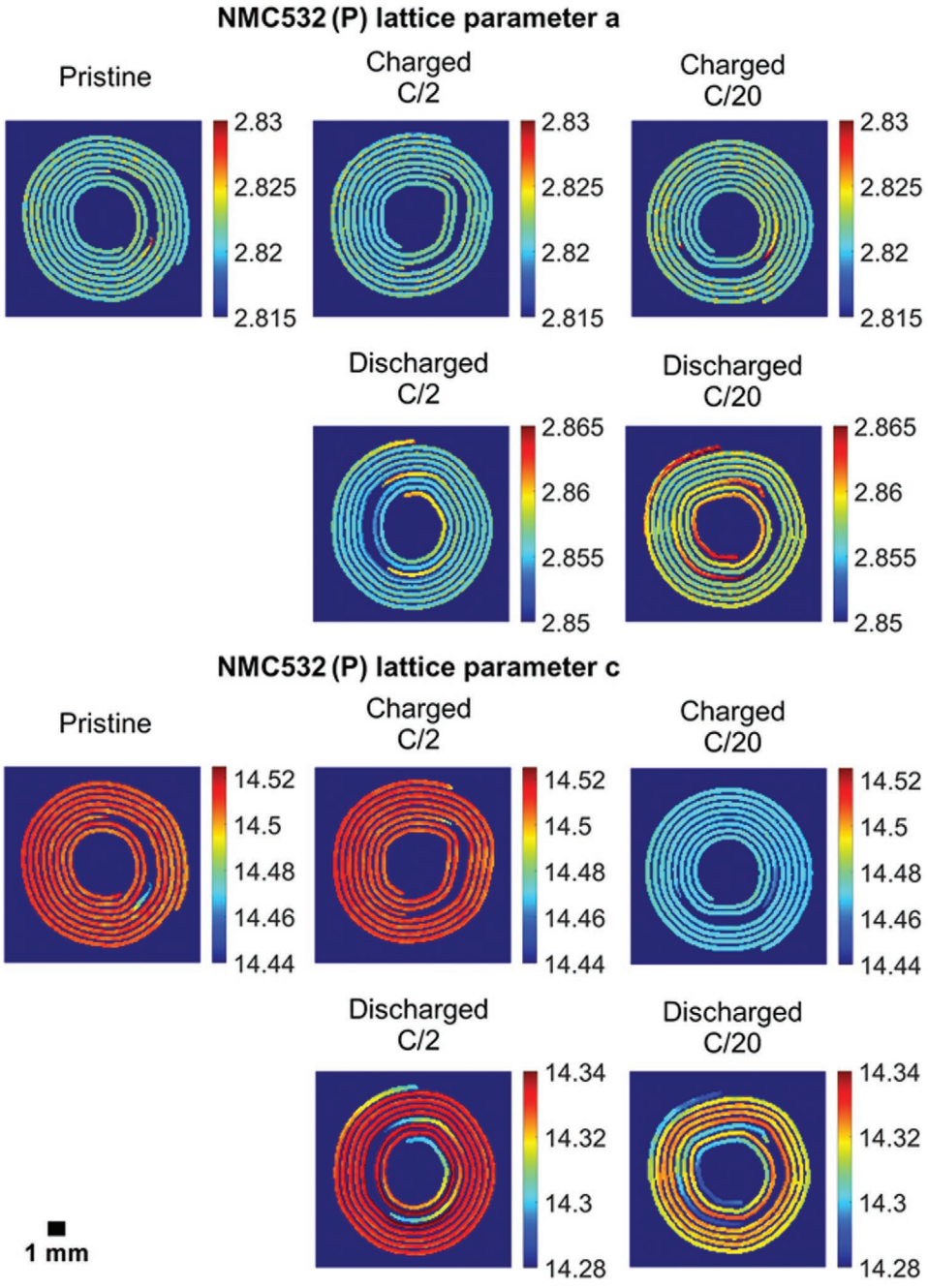

Figure 6. Lattice parameter a (top panel) and c maps (bottom panel) for the primary hexagonal NMC532 phase obtained with the DLSR algorithm. Colorbar units correspond to Å.

Tables S6 and S7, Supporting Information. The lattice parameter maps for the pristine and the two discharged-charged cells follow uniform distributions with the values being the same for the pristine cell (lattice parameter *a* equal to 2.822 Å and *c* to 14.507 Å) and the cell cycled with the higher rate of C/2 (lattice parameter *a* equal to 2.822 Å and *c* to 14.508 Å). On the other hand, the lattice parameter *c* in the cell cycled at C/20 was lower than the lattice parameter *c* in both the pristine cell and the cell charged at the C/2 rate (i.e., 14.472 Å vs 14.507 Å respectively). This variation can be explained by the degree of delithiation in the hexagonal phase which is significantly higher in the case of the cell cycled at the C/20 rate.

For the two discharged cells, there are significant heterogeneities in the distribution of NMC532 lattice parameters. Specifically, these heterogeneities are located in areas close to the Al current collector, the steel casing, and the separator at the core of the jelly roll (Fe-Al-Sep). The absolute values for the lattice parameters for the two cells are slightly different (Tables S6 and S7, Supporting Information); higher *a* lattice parameters and lower *c* lattice parameters were observed for the cell cycled

at C/20 (2.859 and 14.316 Å, respectively) while lower lattice parameters *a* and higher lattice parameters *c* were observed for the cell cycled at C/2 (2.856 and 14.329 Å, respectively). These discrepancies can be explained by the difference in the amount of Li being re-incorporated into the hexagonal structure with a higher amount being present in the cell cycled at the C/20 rate.

3. Discussion

XRD-CT measurements combined with full profile analysis using the Rietveld method revealed numerous heterogeneities in cross-sections of cylindrical commercial LiB cells. Specifically, heterogeneities were observed at the anode in terms of the spatial distribution of the lithiated graphite phases (LiC_6 and LiC_{12} in the charged cells, LiC_{30} and C_6 in the discharged cells) in both the charged and discharged state and at the cathode in terms of lattice parameters of the layered oxide phase at the discharge state. The inhomogeneity of the aforementioned chemical species and physical properties were predominantly observed in the regions close to the Al current collector, the stainless steel casing, and the separator at the core of the jelly roll (Fe-Al-Sep areas). The observed inhomogeneities in these areas are considered to be a result of the cell design (Figure S18, Supporting Information): 1) in the middle of jelly roll the first two layers consist only of separator and anode-Cu, while only later the cathode-Al layer is introduced, 2) in the Al tab region where NMC532 is absent.

At the charged state, these inhomogeneities are primarily identified by the presence of two lithiated graphite phases, LiC_6 and LiC_{12}, for the cell cycled at the C/20 rate. The presence of the less lithiated graphite phase LiC_{12}, was primarily identified at the Fe-Al-Sep regions, where the absence of cathode material coating from neighboring cathode layer(s) negatively impacts the lithiation processes in the anode. Similarly, non-uniform lithium distribution can be a consequence of uneven electrolyte wetting and/or non-uniform current distribution across the cell. As shown in the work of Senyshyn et al.,[51,57] these inhomogeneities across a LiB cylindrical cell can also be observed by mapping the Li content in the Li_xC phases with neutron diffraction imaging, however with several orders of magnitude lower spatial resolution (e.g., 2×2×20 mm compared to 0.02×0.02×0.003 mm in this study).[58] For the cell cycled at the rate of C/2, heterogeneities in the distribution of LiC_{12} and LiC_6 are primarily related to the fast cycling and low charge capacity obtained for this cell, with LiC_6 being formed only at the surface of the anode electrodes. The lithiation profile across the anode shows that lithiation progresses initially from the electrode surface and then further into the thickness of the electrode. Future investigations during battery cycling employing XRD-CT are possible (dynamic experiments). The high spatial resolution images obtained in this work were collected in ca. 1 h; however one can significantly increase the temporal resolution by employing alternative data acquisition approaches, such as the continuous rotation-translation approach, enabling 5D tomographic diffraction imaging experiments.[28,53,59] These results clearly demonstrate the value of chemical imaging and its potential to create new/validate existing electrode, cell, and multi-scale physical models of working Li-ion cylindrical cells which are essential in battery management systems.[60–64]

Regarding the cathode, no variations were observed in the lattice parameters of the layered oxide for either charged cell; this indicates uniform delithiation.

For the discharged cells, both exhibited heterogeneities in the distribution of the lithiated graphite phases in the anode, as well as in the distribution of lattice parameters in the layered oxide in the cathode. In the anode, two crystalline phases were identified, namely LiC_{30} and graphite. The partially lithiated LiC_{30} phase was found to be located in the Fe-Al-Sep regions; limitations during the lithiation process were observed in these regions compared to the rest of the cells, also in the charged cells as discussed previously. At the same time, the distribution of the lattice parameters in the hexagonal NMC532 phase followed a similar trend. Specifically, the cathode composition around the Fe-Al-Sep regions was composed of a crystalline NMC532 phase containing more lithium in its structure than the NMC532 phase present in the other regions of the cell. This suggests that the electrodes around the Fe-Al-Sep regions are experiencing significant inhomogeneities in lithium distribution which is a result of uneven current distribution. Importantly, the effect in these regions is inverted for the materials present in the anode. Specifically, less Li is being incorporated in the graphite anode during charging (i.e., LiC_{12} instead of LiC_6) and less Li is being removed from the anode during discharging (i.e., LiC_{30} instead of graphite); this can significantly affect the cell capacity. As the lithiation process in the Fe-Al-Sep regions differs significantly from the rest of the cell, it is expected that capacity fade during the life cycle of the battery could be directly associated with the degradation processes taking place/originating from these areas. However, it remains to be shown experimentally by investigating the battery under operating conditions and during/after prolonged cycling. Such experiments could also provide a thorough insight into the nature and role of the secondary NMC532 phase; for example, investigating the direct correlation between capacity fade and the quantity (i.e., growth) of this inactive component (i.e., not participating in the (de)lithiation process).

4. Conclusions

XRD-CT combined with the DLSR algorithm enabled, for the first time, spatially-resolved chemical heterogeneities of commercial cylindrical LiBs to be revealed as a function of cycling protocol and cycling rate. We have demonstrated that this technique is able to capture fine details of the various cell components (i.e., steel casing, polymer separator, Al and Cu current collectors) as well as the crystalline phases present in the cathode and anode, with a high spatial resolution (i.e., $20 \times 20 \times 3$ μm^3 voxel size). It should be noted that currently no other technique can achieve this; micro-CT can provide higher spatiotemporal resolution, but cannot differentiate between different Li_xC species or provide information regarding the cathode material (lattice parameters, crystallite size). Neutron diffraction imaging can provide this type of information but with orders of magnitude lower spatiotemporal resolution. The physico-chemical properties of all crystalline materials identified in the LiB cells were obtained using the DLSR algorithm which uses full profile analysis employing the Rietveld method resulting in accurate lattice parameters even

for large samples (i.e., overcoming the parallax artifact). Crystalline phase heterogeneities and their physico-chemical properties induced during cycling protocols demonstrate that XRD-CT is a technique with unique capabilities that provide invaluable insight into the degradation and capacity fade mechanisms of commercial battery cells. Future studies could include operando investigations of LiBs to understand how the distribution of Li and current rates will affect the capacity retention over multiple cycles.

5. Experimental Section

XRD-CT Measurements: XRD-CT measurements were performed at the second experimental hutch (EH2) of beamline P07 at the PETRA III synchrotron at DESY using a 103.5 keV (λ = 0.11979 Å) monochromatic X-ray beam focused to have a spot size of 20×3 µm (Horizontal x Vertical). 2D powder diffraction patterns were collected using the Pilatus3 X CdTe 2 M hybrid photon counting area detector. The battery cells were mounted onto a goniometer which was placed on a rotation stage (Figure S19, Supporting Information). The rotation stage was mounted perpendicularly to a hexapod; the hexapod was used to translate the sample across the beam. The XRD-CT scans were measured by performing a series of zigzag line scans in the z (vertical) direction using the hexapod and rotation steps.

An exposure time of 10 ms and an angular range of 0°–180° with 400 projections in total were used for each XRD-CT dataset. Five zig-zag XRD-CT datasets were acquired in total using the same translation step size (20 microns) continuous translation (fast axis) and stepped rotation (slow axis).[65] The translation steps for the five XRD-CT datasets were the following: 1) Pristine: 549, 2) Charged C/2: 569, 3) Charged C/20: 629, 4) Discharged C/2: 579, and 5) Discharged C/20: 569. These differences were a result of the tomographic alignment process. The detector calibration was performed using a CeO_2 standard (Figure S20, Supporting Information). Every 2D diffraction image was calibrated and azimuthally integrated to a 1D powder diffraction pattern with a 10% trimmed mean filter using the pyFAI software package and in-house developed scripts.[66–68] The integrated diffraction patterns were reshaped into sinograms and centered; the air scatter signal was subtracted from the data. For the conventional data analysis approach, the final XRD-CT images (i.e., reconstructed data volume) were reconstructed using the filtered back projection algorithm. The voxel size in the reconstructed images corresponds to 20 × 20 × 3 μm^3. After the full profile analysis, the maps for the various datasets were aligned and cropped to the same image size (i.e., 520 × 520 pixels).

Full Profile Analysis: Quantitative Rietveld refinement was performed on the reconstructed diffraction patterns with the TOPAS software, on a voxel-by-voxel basis. The results from the refinements were imported into MATLAB in order to create the various figures presented in this work (i.e., phase distribution maps based on the scale factors, weight percentages, and lattice parameters). Rietveld analysis was initially performed using the summed diffraction pattern of each XRD-CT dataset to provide the starting model (Figures S21–S25, Supporting Information) before running the voxel-by-voxel Rietveld analysis to provide the spatially-resolved information. A mask was applied so that only the pixels in the images corresponding to sample regions would be processed (decreasing significantly the number of patterns to be analyzed in each line). A pseudo-voigt peak shape function was used for the refinements after the analysis of the CeO_2 pattern. The parameters refined were the scale factor and lattice parameter for each phase. The diffraction peaks were very sharp for all phases leading to large values for crystallite sizes so these parameters were kept constant during the refinement process. No indication of strain was observed in the data and as a result, it was not added to the model. A single pseudo-voigt peak was used to model the peak generated by the semi-crystalline separator component; in the spatially-resolved analysis, the area and position of the peak were refined while the peak shape was kept constant.

Self-Absorption Correction: The XRD-CT data were first analyzed using the conventional approach; the images were reconstructed using the filtered back projection algorithm and then full profile analysis of the local diffraction patterns was performed using the Rietveld method. This type of analysis can lead to accurate scale factor and weight fraction maps for the various crystalline components in the sample but not lattice parameter/crystallite size maps due to the parallax artifact present in the data. The weight fraction maps obtained from the Rietveld analysis were used to simulate an absorption map using the X-ray mass attenuation coefficient from NIST.[69] This µ attenuation map was then used to correct the XRD-CT sinogram data for self-absorption using the zero-order approximation (Figures S5 and S6, Supporting Information).[70] This process was followed for all five XRD-CT datasets. The self-absorption corrected XRD-CT sinograms were then used for the conventional (i.e., reconstruction using the filtered back projection algorithm followed by full profile analysis of the local diffraction patterns) and the DLSR analysis (after downscaling the sinograms by a factor of four).

DLSR Analysis: Due to the memory expensive requirements of the DLSR approach, the data had to be downscaled by a factor of four to ca. 140 × 140 pixels. This means that the pixel size in the reconstructed DLSR maps corresponds to 80 microns. The downscaled sinograms (containing parallax artifact) were used to reconstruct images using the conventional approach and perform analysis using the Rietveld method. To stabilize the DLSR refinements, the scale factor maps obtained from the conventional analysis were used as inputs to the DLSR and only one global scale factor was refined per crystalline phase (i.e., the distribution of the components was forced to be the one obtained from the conventional approach but a scale factor was applied to these maps which were refined during the DLSR analysis). A mask was created for each phase based on these scale factor maps which allowed to decrease the number of structures needed to be refined (e.g., pixels in the scale factor maps that did not contain Fe did not contain an Fe structure during the DLSR refinement process). It should be noted that without these advances in the DLSR scripts it would be computationally impossible to perform the refinements even with high spec workstation PCs for this resolution (ca. 140×140 pixels). The lattice parameters of the NMC532 (P) were refined spatially; one global lattice parameter was used for the rest of the phases (e.g., the lattice parameter of Fe, Cu, Al should not be varying spatially). Similarly, one global crystallize size parameter was refined for each phase. A 3XS Data Science Workstation C264 × 2 with 2x Intel Xeon Silver 4216 and 350 GB RAM was used to perform the refinements for both the conventional approach (FBP-Rietveld) and the DLSR. After the DLSR analysis, the maps for the various datasets were aligned and cropped to the same image size (i.e., 132 × 132 pixels). The Rwp errors from both the DLSR and the conventional FBP-Rietveld approach are presented in Figures S26–S28 and Tables S8 and S9, Supporting Information.

Electrochemical Testing and Sample Description: Five TF10440 600 mAh 3.7 V batteries (AAA) produced by Trustfire were investigated in this work. The dimensions of the cells were specified as 10.17 × 46.22 mm (diameter × height). The composition of the cathode electrode was determined with ex situ X-ray fluorescence spectroscopy measurements (Figures S2 and S3 and Table S1, Supporting Information). The elemental analysis revealed that the cathode consists of $LiNi_{0.5}Mn_{0.3}Co_{0.2}O_2$ (NMC532). All electrochemical testing was carried out on a Gamry Interface 1000 Potentiostat (Gamry Instruments, USA). Initially, four cells were charged to 4.2 V using a CCCV regime at C/20, holding at 4.2 V until the current decayed to < 5% of the applied current. Two cells were then discharged at C/20 and two cells were discharged at C/2 to 2.75 V. One cell from each set was further charged at the same rate (i.e., C/20 or C/2) to 4.2 V. It should be noted that the experimental capacity of the cells cycled with the slow C/20 rate was 300–350 mAh. Deviations from the 600 mAh capacity claimed by Trustfire likely include the quality of electrode manufacture (adherence, e^- and Li^+ conductivity, quantity of active material), quality of the active electrode materials (functional rather than theoretical capacity and resistance to degradation), and robustness of the electrolyte (mass transport and degradation properties).

Supporting Information

Supporting Information is available from the Wiley Online Library or from the author.

Acknowledgements

The authors acknowledge DESY (Hamburg, Germany), a member of the Helmholtz Association HGF, for the provision of experimental facilities. Parts of this research were carried out at PETRA III. Finden acknowledges funding through the Innovate UK Analysis for Innovators (A4i) program (Project No: 106003). A.M.B. acknowledges funding from EPSRC, grant awards EP/S016481/1 & EP/R026939/1. J.A.D. and T.A. acknowledge funding from the JUICED energy Hub (EP/R023662/1). The authors would like to thank Dr. Leigh Connor from the Diamond Light Source for acquiring the micro-CT data at beamline I12 during an industrial beamtime.

Conflict of Interest

The authors declare no conflict of interest.

Author Contributions

A.V. and D.M. contributed equally to this work. A.V., D.M., T.A., and D.B. conceived the experiment. The XRD-CT measurements were performed by A.V., Y.O., S.W.T.P., and S.D.M.J. The laboratory electrochemical testing and X-ray fluorescence spectroscopy measurements were performed by T.A. O.G., A.C.D., and M.Z. were responsible for P07 instrumentation and setup at the PETRA III, DESY. The MATLAB/TOPAS-DLSR scripts were developed and optimized by A.V. and A.A.C. The XRD-CT data were analyzed by A.V. and D.M. with contributions from H.D., K.B., D.B., J.D., S.D.M.J., and A.M.B. A.V., D.M., and T.A. are responsible for writing the manuscript with contributions and feedback given by all contributors. S.D.M.J., A.M.B., and A.V. directed the research.

Data Availability Statement

Copies of the raw sinogram XRD-CT data can be found at https://doi.org/10.5281/zenodo.5172058. All other data are available from the corresponding authors on reasonable request.

Keywords

diffraction, Li-ion batteries, tomography, X-ray diffraction computed tomography

Received: May 14, 2021
Revised: June 29, 2021
Published online:

[1] V. Etacheri, R. Marom, R. Elazari, G. Salitra, D. Aurbach, *Energy Environ. Sci.* **2011**, *4*, 3243.
[2] G. Zubi, R. Dufo-López, M. Carvalho, G. Pasaoglu, *Renewable Sustainable Energy Rev.* **2018**, *89*, 292.
[3] M. Li, J. Lu, Z. Chen, K. Amine, *Adv. Mater.* **2018**, *30*, 1800561.
[4] J. Xu, F. Lin, M. M. Doeff, W. Tong, *J. Mater. Chem. A* **2017**, *5*, 874.
[5] A. Kraytsberg, Y. Ein-Eli, *Adv. Energy Mater.* **2012**, *2*, 922.
[6] N. Nitta, F. Wu, J. T. Lee, G. Yushin, *Mater. Today* **2015**, *18*, 252.
[7] P. P. R. M. L. Harks, F. M. Mulder, P. H. L. Notten, *J. Power Sources* **2015**, *288*, 92.
[8] F. C. Strobridge, B. Orvananos, M. Croft, H.-C. Yu, R. Robert, H. Liu, Z. Zhong, T. Connolley, M. Drakopoulos, K. Thornton, C. P. Grey, *Chem. Mater.* **2015**, *27*, 2374.
[9] K. Romanenko, P. W. Kuchel, A. Jerschow, *Chem. Mater.* **2020**, *32*, 2107.
[10] K. Suzuki, A. Suzuki, T. Ishikawa, M. Itou, H. Yamashige, Y. Orikasa, Y. Uchimoto, Y. Sakurai, H. Sakurai, *J. Synchrotron Radiat.* **2017**, *24*, 1006.
[11] S. -M. Bak, Z. Shadike, R. Lin, X. Yu, X.-Q. Yang, *NPG Asia Mater.* **2018**, *10*, 563.
[12] Y. Zhang, Z. Yang, C. Tian, *J. Mater. Chem. A* **2019**, *7*, 23628.
[13] Y. Yuan, K. Amine, J. Lu, R. Shahbazian-Yassar, *Nat. Commun.* **2017**, *8*, 15806.
[14] J. Liu, M. Kunz, K. Chen, N. Tamura, T. J. Richardson, *J. Phys. Chem. Lett.* **2010**, *1*, 2120.
[15] M. Ebner, F. Marone, M. Stampanoni, V. Wood, *Science* **2013**, *342*, 716.
[16] K. M. Ø. Jensen, X. Yang, J. V. Laveda, W. G. Zeier, K. A. See, M. Di Michiel, B. C. Melot, S. A. Corr, S. J. L. Billinge, *J. Electrochem. Soc.* **2015**, *162*, A1310.
[17] T. Sasaki, C. Villevieille, Y. Takeuchi, P. Novák, *Adv. Sci.* **2015**, *2*, 1500083.
[18] J. Wang, Yu-C Karen Chen-Wiegart, C. Eng, Q. Shen, J. Wang, *Nat. Commun.* **2016**, *7*, 12372.
[19] J. Lim, Y. Li, D. H. Alsem, H. So, S. C. Lee, P. Bai, D. A. Cogswell, X. Liu, N. Jin, Y.-S. Yu, N. J. Salmon, D. A. Shapiro, M. Z. Bazant, T. Tyliszczak, W. C. Chueh, *Science* **2016**, *353*, 566.
[20] P. Pietsch, M. Hess, W. Ludwig, J. Eller, V. Wood, *Sci. Rep.* **2016**, *6*, 27994.
[21] P. Pietsch, V. Wood, *Annu. Rev. Mater. Res.* **2017**, *47*, 451.
[22] Y. Xu, E. Hu, K. Zhang, X. Wang, V. Borzenets, Z. Sun, P. Pianetta, X. Yu, Y. Liu, X.-Q. Yang, H. Li, *ACS Energy Lett.* **2017**, *2*, 1240.
[23] Y.-S. Yu, M. Farmand, C. Kim, Y. Liu, C. P. Grey, F. C. Strobridge, T. Tyliszczak, R. Celestre, P. Denes, J. Joseph, H. Krishnan, F. R. N. C. Maia, A. L. D Kilcoyne, S. Marchesini, T. P. C. Leite, T. Warwick, H. Padmore, J. Cabana, D. A. Shapiro, *Nat. Commun.* **2018**, *9*, 921.
[24] M. J. Mühlbauer, A. Schökel, M. Etter, V. Baran, A. Senyshyn, *J. Power Sources* **2018**, *403*, 49.
[25] X. Yu, Z. Feng, Y. Ren, D. Henn, Z. Wu, K. An, B. Wu, C. Fau, C. Li, S. J. Harris, *J. Electrochem. Soc.* **2018**, *165*, A1578.
[26] C. Tian, Y. Xu, D. Nordlund, F. Lin, J. Liu, Z. Sun, Y. Liu, M. Doeff, *Joule* **2018**, *2*, 464.
[27] V. Wood, *Nat. Rev. Mater.* **2018**, *3*, 293.
[28] H. Liu, S. Kazemiabnavi, A. Grenier, G. Vaughan, M. Di Michiel, B. J. Polzin, K. Thornton, K. W. Chapman, P. J. Chupas, *ACS Appl. Mater. Interfaces* **2019**, *11*, 18386.
[29] D. P. Finegan, A. Vamvakeros, L. Cao, C. Tan, T. M. M. Heenan, S. R. Daemi, S. D. M. Jacques, A. M. Beale, M. Di Michiel, K. Smith, D. J. L. Brett, P. R. Shearing, C. Ban, *Nano Lett.* **2019**, *19*, 3811.
[30] D. P. Finegan, A. Vamvakeros, C. Tan, T. M. M. Heenan, S. R. Daemi, N. Seitzman, M. Di Michiel, S. Jacques, A. M. Beale, D. J. L. Brett, P. R. Shearing, K. Smith, *Nat. Commun.* **2020**, *11*, 631.
[31] T. M. M. Heenan, C. Tan, J. Hack, D. J. L. Brett, P. R. Shearing, *Mater. Today* **2019**, *31*, 69.
[32] R. F. Ziesche, T. Arlt, D. P. Finegan, T. M. M. Heenan, A. Tengattini, D. Baum, N. Kardjilov, H. Markötter, I. Manke, W. Kockelmann, D. J. L. Brett, P. R. Shearing, *Nat. Commun.* **2020**, *11*, 777.
[33] S. Müller, M. Lippuner, M. Verezhak, V. De Andrade, F. De Carlo, V. Wood, *Adv. Energy Mater.* **2020**, *10*, 1904119.
[34] Y. Kimura, A. Tomura, M. Fakkao, T. Nakamura, N. Ishiguro, O. Sekizawa, K. Nitta, T. Uruga, T. Okumura, M. Tada, Y. Uchimoto, K. Amezawa, *J. Phys. Chem. Lett.* **2020**, *11*, 3629.

[35] Y. Kimura, M. Fakkao, T. Nakamura, T. Okumura, N. Ishiguro, O. Sekizawa, K. Nitta, T. Uruga, M. Tada, Y. Uchimoto, K. Amezawa, *ACS Appl. Energy Mater.* **2020**, *3*, 7782.
[36] T. M. M. Heenan, D. P. Finegan, B. Tjaden, X. Lu, F. Iacoviello, J. Millichamp, D. J. L. Brett, P. R. Shearing, *Nano Energy* **2018**, *47*, 556.
[37] A. Pfrang, A. Kersys, A. Kriston, D. U. Sauer, C. Rahe, S. Käbitz, E. Figgemeier, *J. Power Sources* **2018**, *392*, 168.
[38] X. Lu, A. Bertei, D. P. Finegan, C. Tan, S. R. Daemi, J. S. Weaving, K. B. O'regan, T. M. M. Heenan, G. Hinds, E. Kendrick, D. J. L. Brett, P. R. Shearing, *Nat. Commun.* **2020**, *11*, 2079.
[39] N. Sharma, V. K. Peterson, M. M. Elcombe, M. Avdeev, A. J. Studer, N. Blagojevic, R. Yusoff, N. Kamarulzaman, *J. Power Sources* **2010**, *195*, 8258.
[40] X.-L. Wang, K. An, L. Cai, Z. Feng, S. E. Nagler, C. Daniel, K. J. Rhodes, A. D. Stoica, H. D. Skorpenske, C. Liang, W. Zhang, J. Kim, Y. Qi, S. J. Harris, *Sci. Rep.* **2012**, *2*, 747.
[41] H. Zhou, K. An, S. Allu, S. Pannala, J. Li, H. Z. Bilheux, S. K. Martha, J. Nanda, *ACS Energy Lett.* **2016**, *1*, 981.
[42] C. Von Lüders, V. Zinth, S. V. Erhard, P. J. Osswald, M. Hofmann, R. Gilles, A. Jossen, *J. Power Sources* **2017**, *342*, 17.
[43] N. Paul, J. Keil, F. M. Kindermann, S. Schebesta, O. Dolotko, M. J. Mühlbauer, L. Kraft, S. V. Erhard, A. Jossen, R. Gilles, *J. Energy Storage* **2018**, *17*, 383.
[44] S. Schweidler, L. De Biasi, A. Schiele, P. Hartmann, T. Brezesinski, J. Janek, *J. Phys. Chem. C* **2018**, *122*, 8829.
[45] J. K. Mathiesen, R. E. Johnsen, A. S. Blennow, P. Norby, *Carbon* **2019**, *153*, 347.
[46] D. R. Sørensen, M. Heere, J. Zhu, M. S. D. Darma, S. M. Zimnik, M. J. Mühlbauer, L. Mereacre, V. Baran, A. Senyshyn, M. Knapp, H. Ehrenberg, *ACS Appl. Energy Mater.* **2020**, *3*, 6611.
[47] J. Zhu, M. Knapp, D. R. Sørensen, M. Heere, M. S. D. Darma, M. Müller, L. Mereacre, H. Dai, A. Senyshyn, X. Wei, H. Ehrenberg, *J. Power Sources* **2021**, *489*, 229422.
[48] V. Kochetov, M. J. Mühlbauer, A. Schökel, T. Fischer, T. Müller, M. Hofmann, P. Staron, U. Lienert, W. Petry, A. Senyshyn, *J. Phys.: Condens. Matter* **2020**, *33*, 105901.
[49] M. J. Mühlbauer, D. Petz, V. Baran, O. Dolotko, M. Hofmann, R. Kostecki, A. Senyshyn, *J. Power Sources* **2020**, *475*, 228690.
[50] D. Petz, M. J. Mühlbauer, V. Baran, M. Frost, A. Schökel, C. Paulmann, Y. Chen, D. Garcés, A. Senyshyn, *J. Power Sources* **2020**, *448*, 227466.
[51] A. Senyshyn, M. J. Mühlbauer, O. Dolotko, M. Hofmann, H. Ehrenberg, *Sci. Rep.* **2015**, *5*, 18380.
[52] D. S. Wragg, M. G. O'brien, M. Di Michiel, F. Lønstad-Bleken, *J. Appl. Crystallogr.* **2015**, *48*, 1719.
[53] A. Vamvakeros, S. D. M. Jacques, M. Di Michiel, D. Matras, V. Middelkoop, I. Z. Ismagilov, E. V. Matus, V. V. Kuznetsov, J. Drnec, P. Senecal, A. M. Beale, *Nat. Commun.* **2018**, *9*, 4751.
[54] N. K. Wittig, J. Palle, M. Østergaard, S. Frølich, M. E. Birkbak, K. M. Spiers, J. Garrevoet, H. Birkedal, *ACS Nano* **2019**, *13*, 12949.
[55] J. Sottmann, M. Di Michiel, H. Fjellvåg, L. Malavasi, S. Margadonna, P. Vajeeston, G. B. M. Vaughan, D. S. Wragg, *Angew. Chem., Int. Ed.* **2017**, *56*, 11385.
[56] A. Vamvakeros, A. A. Coelho, D. Matras, H. Dong, Y. Odarchenko, S. W. T. Price, K. T. Butler, O. Gutowski, A. -C. Dippel, M. Zimmermann, I. Martens, J. Drnec, A. M. Beale, S. D. M. Jacques, *J. Appl. Crystallogr.* **2020**, *53*, 1531.
[57] M. J. Mühlbauer, O. Dolotko, M. Hofmann, H. Ehrenberg, A. Senyshyn, *J. Power Sources* **2017**, *348*, 145.
[58] A. Senyshyn, M. J. Mühlbauer, O. Dolotko, M. Hofmann, T. Pirling, H. Ehrenberg, *J. Power Sources* **2014**, *245*, 678.
[59] D. Matras, A. Vamvakeros, S. D. M. Jacques, M. Di Michiel, V. Middelkoop, I. Z. Ismagilov, E. V. Matus, V. V. Kuznetsov, R. J. Cernik, A. M. Beale, *J. Mater. Chem. A* **2021**, *9*, 11331.
[60] C. D. Rahn, C. Y. Wang, *Battery Systems Engineering*, Wiley, West Sussex, UK **2013**.
[61] A. A. Franco, A. Rucci, D. Brandell, C. Frayret, M. Gaberscek, P. Jankowski, P. Johansson, *Chem. Rev.* **2019**, *119*, 4569.
[62] A. Mistry, K. Smith, P. P. Mukherjee, *ACS Appl. Mater. Interfaces* **2020**, *12*, 16359.
[63] H. Xu, J. Zhu, D. P. Finegan, H. Zhao, X. Lu, W. Li, N. Hoffman, A. Bertei, P. Shearing, M. Z. Bazant, *Adv. Energy Mater.* **2021**, *11*, 2003908.
[64] M.-C. Pang, K. Yang, R. Brugge, T. Zhang, X. Liu, F. Pan, S. Yang, A. Aguadero, B. Wu, M. Marinescu, H. Wang, G. J. Offer, *Mater. Today* **2021**, https://doi.org/10.1016/j.mattod.2021.02.011.
[65] A. Vamvakeros, S. D. M. Jacques, M. Di Michiel, P. Senecal, V. Middelkoop, R. J. Cernik, A. M. Beale, *J. Appl. Crystallogr.* **2016**, *49*, 485.
[66] A. Vamvakeros, S. D. M. Jacques, M. Di Michiel, V. Middelkoop, C. K. Egan, R. J. Cernik, A. M. Beale, *J. Appl. Crystallogr.* **2015**, *48*, 1943.
[67] G. Ashiotis, A. Deschildre, Z. Nawaz, J. P. Wright, D. Karkoulis, F. E. Picca, J. Kieffer, *J. Appl. Crystallogr.* **2015**, *48*, 510.
[68] A. Vamvakeros, *nDTomo Software Suite*. **2018**, https://github.com/antonyvam/nDTomo.
[69] P. J. Linstrom, W. G. Mallard, *NIST Chemistry WebBook. NIST Stand. Ref. Database Number 69*, https://doi.org/10.18434/T4D303.
[70] A. Vamvakeros, D. Matras, S. D. M. Jacques, M. Di Michiel, V. Middelkoop, P. Cong, S. W. T. Price, C. L. Bull, P. Senecal, A. M. Beale, *Catal. Today* **2021**, *364*, 242.